Analysis of the shape of a subwavelength focal spot for the linearly polarized light

Victor V. Kotlyar,[1] Sergey S. Stafeev,[1,*] Yikun Liu,[2,3]
Liam O'Faolain,[2] and Alexey A. Kovalev[1]

[1]Image Processing Systems Institute of the Russian Academy of Sciences, Samara 443001, Russia

[2]SUPA, School of Physics and Astronomy, University of St. Andrews, St. Andrews KY16 9SS, UK

[3]State Key Laboratory of Optoelectronic Materials and Technologies, Sun Yat-sen University, Guangzhou 510275, China

*Corresponding author: sergey.stafeev@gmail.com

By decomposing a linearly polarized light field in terms of plane waves, the elliptic intensity distribution across the focal spot is shown to be determined by the E-vector's longitudinal component. Considering that the Poynting vector's projection onto the optical axis (power flux) is independent of the E-vector's longitudinal component, the power flux cross section has a circular form. Using a near-field scanning optical microscope (NSOM) with a small-aperture metal tip, we show that a glass zone plate (ZP) having a focal length of one wavelength focuses a linearly polarized Gaussian beam into a weak ellipse with the Cartesian axis diameters $\text{FWHM}_x = (0.44 \pm 0.02)\lambda$ and $\text{FWHM}_y = (0.52 \pm 0.02)\lambda$ and the (depth of focus) $\text{DOF} = (0.75 \pm 0.02)\lambda$, where λ is the incident wavelength. The comparison of the experimental and simulation results suggests that NSOM with a hollow pyramidal aluminum-coated tip (with 70° apex and 100 nm diameter aperture) measures the transverse intensity, rather than the power flux or the total intensity. The conclusion that the small-aperture metal tip measures the transverse intensity can be inferred from the Bethe–Bouwkamp theory. © 2013 Optical Society of America

OCIS codes: 050.1380, 180.4243.

1. Introduction

The subwavelength focusing of light by means of micro-optics elements remains a highly relevant problem because the tighter focal spot not only produces a higher resolution in applications, such as lithography, microscopy, and optical memory, but also increases the radiation power density, which is important for micromanipulation. In recent years, significant advances have been reported in this area. By way of illustration, the subwavelength focusing has been performed using planar plasmonic structures [1,2] or plasmonic lenses [3,4]. The tight focusing of laser light can also be achieved in the near-surface regions of conventional optical elements like a microaxicon [5], a ZP [6,7], a microlens [8], a solid immersion lens [9], and a conventional high NA lens [10–13]. The subwavelength focal spot can also be obtained on the tip of dielectric and metallic microcones [14–16]. The micro-optics elements can be utilized not only for subwavelength focusing but also for nanoimaging [17].

Note, however, that the above-cited articles have not been concerned with processes whereby the near-field radiation is registered using a near-field scanning optical microscope (NSOM) small-aperture tip. The following questions have remained unanswered so far. Which radiation component—the power density or the power flux—is being registered by the near-field microscope? Why for the linearly polarized light is the focal spot intensity in the form of an ellipse, whereas the Poynting vector's optical-axis projection (power flux) is focused into a circle?

Also, the publications quoted above lack the comparative analysis of the experimental data on the subwavelength focal spot measurements and the results of the rigorous simulation based on Maxwell's equations.

The detection of the radiation component in the focal region with an NSOM has been intensively conducted previously [18–21]. This field is still under debate. In [18] a golden conic tip with a 30° apex and a 10 nm radius placed close to the glass substrate was illuminated by a strongly focused laser mode of wavelength $\lambda = 830$ nm and NA = 1.4. It was shown to be sensitive only to the longitudinal E-field component. The experiment was concerned with measuring the intensity of the second harmonic generated by the golden tip, which was found to be proportional to the squared intensity of the incident field longitudinal component. In [19], an NSOM aluminum tapered fiber tip with a ~60 nm aperture was used to measure the focal spot of a linearly polarized laser beam of wavelength $\lambda = 633$ nm and NA = 1.65: FWHM = 0.43λ (across the polarization axis) and FWHM = 0.66λ (along the polarization axis). The discrepancy between the theory and the experiment was 5%. The result has shown the probe to be equally sensitive to the longitudinal and transverse field components. Unfortunately, the authors have failed to indicate the probe apex. In addition, the generation of the focal spot of evanescent waves in the vicinity of the substrate surface (refractive index is $n = 1.78$) by means of an annular aperture was reported in [19]. The focus measurement conducted with the same NSOM probe showed the probe to be three times more sensitive to the longitudinal E-field component $|E_z|$ than to the transverse component $|E_x|$, i.e., $|E_{\text{det}}|^2 = |E_x|^2 + 3|E_z|^2$. In [20], the focal spot generated by a radially polarized laser beam of wavelength $\lambda = 633$ nm and NA = 1.65 was measured using the same NSOM as in [19]. The theoretical and experimental values of the circular focal spot size were found to be nearly the same: FWHM = 0.33λ or, with regard for the numerical aperture, FWHM = $0.54\lambda/\text{NA}$. Note that the longitudinal component was found to account for 70% of the total intensity of the focus from the radially polarized field. One can infer that the probe of [20] is predominantly sensitive to the longitudinal field component. Meanwhile, an opposite result was reported in [21]. The NSOM with a metal-plated tip measured the focus from a plasmon polariton generated by an annular slit in a metallic film. Although the longitudinal focal component was estimated to be 10 times larger than the transverse component ($|E_z|/|E_x| \sim 10$), only the transverse component $|E_x|$ was experimentally detected. Unfortunately, the geometry of the probe was not discussed in [21]. From this brief overview [18–21] we can infer that when using an NSOM to detect the electromagnetic field the properties of the probe play a crucial role. The coupling of different field components appears to be largely determined by the geometry of the probe (etching angle, coating thickness, the aperture size). Because of this, we provide detailed characteristics of the tip utilized in this paper. The NSOM tip used for the experiment was a tetrahedral pyramid with a 20×20 μm base and a 13 μm height, with the tip apex being 70°. The hollow pyramid was coated with a 500 nm layer of SiO_2 and a 100 nm aluminum layer. The tip apex had an aperture of ~100 nm in diameter (see Fig. 14). It is noteworthy that the experimental results discussed in this work are in agreement with those reported in [21]. Thus, it can be concluded that an NSOM with such type of tip measures only the transverse E-field component, $|E_x|^2$.

In this paper, by decomposing the linearly polarized light field in terms of plane waves we show that the elliptic shape of the intensity cross section is determined by the longitudinal E-field component. Considering that the axial Poynting vector's projection (the power flux) is independent of the said E-vector's longitudinal component, the power flux cross section is a circle. Using an NSOM with a small-aperture metal tip, we experimentally show that a glass binary ZP with a wavelength focal length focuses the linearly polarized Gaussian beam into a weakly elliptical focal spot with the Cartesian axis diameters $\text{FWHM}_x = (0.44 \pm 0.02)\lambda$ and $\text{FWHM}_y = (0.52 \pm 0.02)\lambda$ and the DOF $= (0.75 \pm 0.02)\lambda$, where λ is the incident wavelength. The comparison of the experimental results with the finite-difference time-domain (FDTD)-based numerical simulation suggests an unambiguous conclusion that the NSOM tip measures the transverse intensity (power density) rather than the power flux or the total intensity. The fact that the small-aperture metal tip measures the transverse intensity is in compliance with the Bethe–Bouwkamp theory.

2. Linearly Polarized Light: Focal Spot Intensity and Poynting Vector's Projection

Assume that light is propagating along the optical axis z. Let there be a linearly polarized electromagnetic field with a radial symmetry in the initial plane ($z = 0$):

$$\begin{cases} E_x(r, \varphi, 0) \equiv E_x(r), \\ E_y(r, \varphi, 0) \equiv 0, \\ E_z(r, \varphi, 0) \equiv 0, \end{cases} \tag{1}$$

where (r, φ) are the polar coordinates in the initial plane.

After the propagation through the free space, the light wave will have the following intensity:

$$I = |\mathbf{E}|^2 = |E_x|^2 + |E_y|^2 + |E_z|^2, \tag{2}$$

and the power flux, which is parallel to the optical axis z will be given by

$$S_z = \frac{1}{2} \operatorname{Re}\{(\mathbf{E} \times \mathbf{H}^*)_z\} = \frac{1}{2} \operatorname{Re}\{E_x H_y^* - E_y H_x^*\}. \tag{3}$$

Since $E_y = 0$, Eqs. ([2](#)) and ([3](#)) can be rearranged as

$$I = |E_x|^2 + |E_z|^2, \tag{4}$$

$$S_z = \frac{1}{2}\,\mathrm{Re}\{E_x H_y^*\}. \tag{5}$$

Using Maxwell's equation for the monochromatic light of frequency ω

$$\mathrm{rot}\,\mathbf{E} = -i\omega\mu_0\mu\mathbf{H}, \tag{6}$$

where μ is the permeability and μ_0 is vacuum permeability, we derive from Eq. ([5](#)) that

$$S_z = \mathrm{Re}\left\{\frac{-i}{2\omega\mu_0\mu}E_x\left(\frac{\partial E_x^*}{\partial z} - \frac{\partial E_z^*}{\partial u}\right)\right\}. \tag{7}$$

Let us decompose the E_x-component in terms of the angular spectrum of plane waves:

$$E_x(u,v,z) = \iint_{\mathbb{R}^2} A(\alpha,\beta)\exp\left\{ik\left[\alpha u + \beta v + z\sqrt{1-\alpha^2-\beta^2}\right]\right\}\mathrm{d}\alpha\mathrm{d}\beta, \tag{8}$$

where (u, v, z) are the Cartesian coordinates in space and (α, β) are the Cartesian coordinates in the spectral plane, $k = 2\pi/\lambda$.

From the third Maxwell's equation

$$\frac{\partial E_x}{\partial u} + \frac{\partial E_y}{\partial v} + \frac{\partial E_z}{\partial z} = 0, \tag{9}$$

and considering that $E_y \equiv 0$, the E_z-component is given by

$$E_z(u,v,z) = -\iint_{\mathbb{R}^2} \frac{\alpha}{\sqrt{1-\alpha^2-\beta^2}}A(\alpha,\beta)\exp\left\{ik\left[\alpha u + \beta v + z\sqrt{1-\alpha^2-\beta^2}\right]\right\}\mathrm{d}\alpha\mathrm{d}\beta + C(u,v). \tag{10}$$

The constant $C(u,v)$ that arises from the integration with respect to z, denotes the infinite constant field on the z-axis. From physical considerations, we may put it equal to zero. Also, the expression in the brackets in Eq. ([7](#)) can be rearranged as

$$\frac{\partial E_x^*}{\partial z} - \frac{\partial E_z^*}{\partial u} = -ik \iint_{\mathbb{R}^2} \frac{1-\beta^2}{\sqrt{1-\alpha^2-\beta^2}}A^*(\alpha,\beta) \times \exp\left\{-ik\left[\alpha u + \beta v + z\sqrt{1-\alpha^2-\beta^2}\right]\right\}\mathrm{d}\alpha\mathrm{d}\beta. \tag{11}$$

Considering that the E_x-component is radially symmetric in the initial plane, its angular spectrum is also symmetric, i.e., $A(\zeta, \phi) \equiv A(\zeta)$, where (ζ, ϕ) are the polar coordinates in the spectral plane. Taking this into account, Eqs. ([8](#)), ([10](#)), and ([11](#)) can be rewritten in the polar coordinates. In this case, all the integrals with respect to ϕ will be expressed through the Bessel functions:

$$E_x(\rho,\theta,z) = 2\pi\int_0^\infty A(\zeta)\exp\left(ikz\sqrt{1-\zeta^2}\right)J_0(k\rho\zeta)\zeta\mathrm{d}\zeta, \tag{12}$$

$$E_z(\rho,\theta,z) = -2\pi i\cos\theta\int_0^\infty A(\zeta)\exp\left(ikz\sqrt{1-\zeta^2}\right) \times J_1(k\rho\zeta)\frac{\zeta^2\mathrm{d}\zeta}{\sqrt{1-\zeta^2}}, \tag{13}$$

$$\frac{\partial E_x^*}{\partial z} - \frac{\partial E_z^*}{\partial u} = -2\pi ik\int_0^\infty A^*(\zeta)\exp\left(-ikz\sqrt{1-\zeta^2}\right) \times \left[\left(1-\frac{\zeta^2}{2}\right)J_0(k\rho\zeta) - \frac{\zeta^2}{2}J_2(k\rho\zeta)\cos(2\theta)\right]\frac{\zeta\mathrm{d}\zeta}{\sqrt{1-\zeta^2}}. \tag{14}$$

Substitute Eqs. ([12](#))–([14](#)) into Eqs. ([4](#)) and ([7](#)):

$$I = 4\pi^2\left|\int_0^\infty A(\zeta)\exp\left(ikz\sqrt{1-\zeta^2}\right)J_0(k\rho\zeta)\zeta\mathrm{d}\zeta\right|^2 + 4\pi^2\cos^2\theta\left|\int_0^\infty A(\zeta)\exp\left(ikz\sqrt{1-\zeta^2}\right)J_1(k\rho\zeta)\frac{\zeta^2\mathrm{d}\zeta}{\sqrt{1-\zeta^2}}\right|^2, \tag{15}$$

$$S_z = -\frac{2\pi^2 k}{\omega\mu_0\mu}\,\mathrm{Re}\left(\left\{\int_0^\infty A(\zeta)\exp\left(ikz\sqrt{1-\zeta^2}\right)J_0(k\rho\zeta)\zeta\mathrm{d}\zeta\right\}\left\{\int_0^\infty A^*(\zeta)\exp\left(-ikz\sqrt{1-\zeta^2}\right)\right.\right. \times \left.\left.\left[\left(1-\frac{\zeta^2}{2}\right)J_0(k\rho\zeta) - \frac{\zeta^2}{2}J_2(k\rho\zeta)\cos(2\theta)\right]\frac{\zeta\mathrm{d}\zeta}{\sqrt{1-\zeta^2}}\right\}\right). \tag{16}$$

From Eqs. (15) and (16), the intensity and the power flux are seen to be symmetric about the x-axis, so that they take the same values for any pair of points (ρ, θ) and $(\rho, -\theta)$. It can also be inferred from Eq. (15) that for a specified ρ the intensity is maximal at points $(\rho, 0)$ and (ρ, π) and minimal at $(\rho, \pi/2)$ and $(\rho, 3\pi/2)$. This is the reason why an elliptic focal spot is generated, with the major axis found on the x-axis considering that the polarization is in the xz-plane. Note that the radial symmetry violation is determined by the second term in the intensity expression Eq. (15) and by the second factor in the power flux expression Eq. (16). If the NA is small ($\zeta \ll 1$), the factor $\zeta^2/(1 - \zeta^2)^{-1/2}$ entering the second integral in Eq. (15) tends to zero, preventing the second term from making a significant contribution to the intensity. This explains why the focal spot has a circular shape. If, however, the tight focusing is performed, for an essential proportion of waves of the angular spectrum, the value of ζ will tend to unity. Thus, the second term contribution may become several times greater than that of the first term, leading to the asymmetry, so that the focal spot becomes an ellipse, or even a bone or a dumbbell.

For the power flux, the relation is different. The $\zeta^2/(1 - \zeta^2)^{-1/2}$ factor affects the symmetric and asymmetric parts of the expression in the square brackets in Eq. (16) in the same way. For a small NA ($\zeta \ll 1$), the power flux is determined by the radially symmetric term $(1 - \zeta^2/2)J_0(k\rho\zeta)$. Because of this, when measuring the focal spot's intensity, rather than the power flux, it has a circular form. When the NA is high and ζ tends to unity, both terms in the square brackets make approximately the same contribution. However, the second term's contribution cannot be very much larger than that of the first term. Besides, in the near-focus region ($\rho = 0$) the zero-order Bessel function exerts a greater impact when compared with the second-order Bessel function. Thus, the resulting focal spot is closer to the circle than that measured in terms of intensity.

By way of illustration, below we analyze a Bessel beam with a circular angular spectrum:

$$A(\zeta) = \delta(\zeta - \alpha), \qquad (17)$$

where $\delta(x)$ is the Dirac delta-function and α is the Bessel beam parameter. Thus, instead of the integral relations in Eqs. (15) and (16), we can obtain the explicit relations of the intensity and the power flux:

$$I = [2\pi\alpha J_0(k\alpha\rho)]^2 + \left[\frac{2\pi\alpha^2}{\sqrt{1 - \alpha^2}} J_1(k\alpha\rho)\cos\theta\right]^2, \quad (18)$$

$$S_z = -\frac{2\pi^2 k}{\omega\mu_0\mu} J_0(k\alpha\rho)\left[\left(1 - \frac{\alpha^2}{2}\right)J_0(k\alpha\rho)\right.$$
$$\left. - \frac{\alpha^2}{2}J_2(k\alpha\rho)\cos(2\theta)\right]\frac{\alpha^2}{\sqrt{1 - \alpha^2}}. \qquad (19)$$

To simulate the low NA case, we put $\alpha = 0.3$ (Fig. 1). To simulate the tight focusing, we put $\alpha = 0.8$ (Fig. 2) and $\alpha = 0.9$ (Fig. 3). The intensity and the power flux for different values of α are shown in Figs. 1–3: the x-axis is horizontal and the y-axis is vertical. The rest simulation parameters are: the wavelength $\lambda = 532$ nm, the distance $z = 10\lambda$, and the simulation domains $-5\lambda \leq x \leq 5\lambda$, $-5\lambda \leq y \leq 5\lambda$.

Figures 1–3 confirm the above-made assumptions. With increasing numerical aperture, the focal spot measured for the intensity is, at first, a circle, then, becomes an ellipse, finally acquiring a dumbbell form. Note that for the power flux, the focal spot always remains close to a circle [in Fig. 3(b)], being described by a weak ellipse elongated along the y-axis, as can easily be seen from Eq. (19). From Figs. 2 and 3, the focal spot sizes for the intensity and the
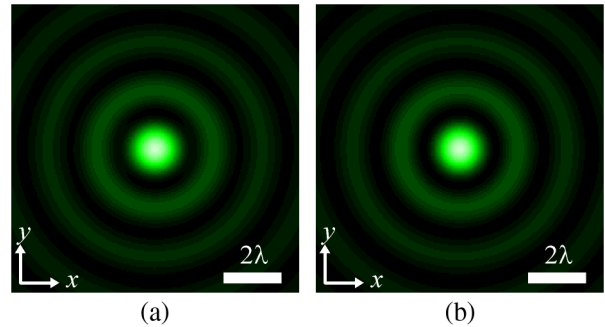

Fig. 1. (Color online) Patterns of (a) the intensity and (b) the power flux for the Bessel beam at $\alpha = 0.3$.
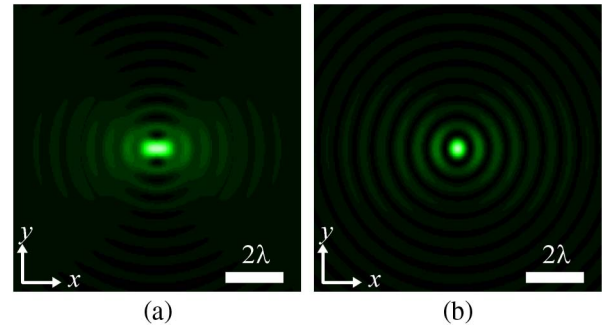

Fig. 2. (Color online) Patterns of (a) the intensity and (b) the power flux for the Bessel beam at $\alpha = 0.8$.
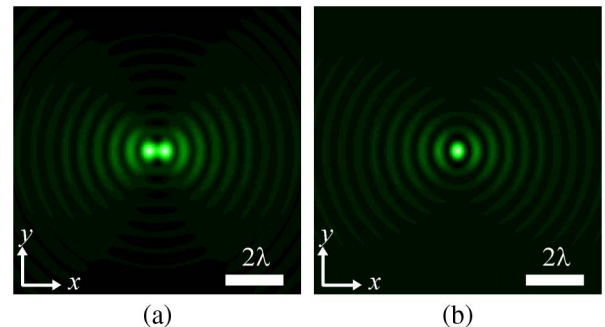

Fig. 3. (Color online) Patterns of (a) the intensity and (b) the power flux for the Bessel beam at $\alpha = 0.9$.

power flux measured along the vertical axis are seen to be close to each other. From Fig. 3, the power flux is seen to generate a weak elliptical focal spot with $\text{FWHM}_x = 0.36\lambda$ and $\text{FWHM}_y = 0.44\lambda$, whereas the intensity is focused in a bone-like spot with the Cartesian axis diameters of $\text{FWHM}_x = 0.98\lambda$ and $\text{FWHM}_y = 0.40\lambda$.

3. Tight Focusing of Linearly Polarized Light with a Subwavelength Binary Axicon

In Section 1, the propagation of a linearly polarized field with the initial amplitude described by the Bessel function was simulated using Eqs. (18) and (19). In this section, we address the inverse problem of generating a linearly polarized Bessel beam with a binary microaxicon using the FDTD-based simulation. We demonstrate that the diffraction patterns have the same structure in both cases.

Fig. 4. (Color online) Contour map of the binary microaxicon of period $T = \lambda$ in the calculated field (the rings have $n = 1.52$, while the background has $n = 1$).

We aim to simulate the propagation of a linearly polarized Gaussian beam of wavelength $\lambda = 532$ nm and waist radius $\omega = 7\lambda$ through a binary microaxicon of radius $R = 8$ μm, period $T = \lambda$ (see Fig. 4), refractive index $n = 1.52$, and height $h = 532$ nm. The simulation was conducted using the FDTD-based FullWAVE software [22], the grid quantization was $\lambda/50$ in space and $\lambda/100c$ in time, where c is the speed of light in free space. It is noteworthy that when calculating the power flux instead of the intensity, the resulting focal spot is a circle (rather than an ellipse) whose diameter is somewhat larger than the minor diameter of the intensity ellipse.

Figure 5(a) shows an adjacent two-dimensional (gray-level) intensity pattern generated by the binary microaxicon of period $T = \lambda = 532$ nm (Fig. 4), while Fig. 5(b) shows the power flux in the same plane.

From Fig. 5, the power flux is seen to generate a circular focal spot with $\text{FWHM} = 0.36\lambda$, whereas the intensity is focused in an elliptic spot with the Cartesian axis diameters of $\text{FWHM}_x = 0.75\lambda$ and $\text{FWHM}_y = 0.30\lambda$. The reason is that the E-field's longitudinal component E_z does not contribute to the Poynting vector's longitudinal component. The E_z component arises in the polarization plane XZ when the rays are converging in focus. In the perpendicular plane YZ, the E_z component does not arise when the rays are converging in focus. The focal spot patterns in Figs. 5 and 3 are seen to be in a qualitative agreement. For instance, the ratio of the major axis to the minor axis of the ellipse in Fig. 3(a) is $0.98\lambda/0.40\lambda = 2.45$, which is nearly the same as that for the ellipse in Fig. 5(a): $0.75\lambda/0.30\lambda = 2.5$.

4. Tight Focusing of the Linearly Polarized Light Using a Zone Plate

A. Simulation

In this section, we analyze focusing a linearly polarized Gaussian beam of wavelength $\lambda = 532$ nm and
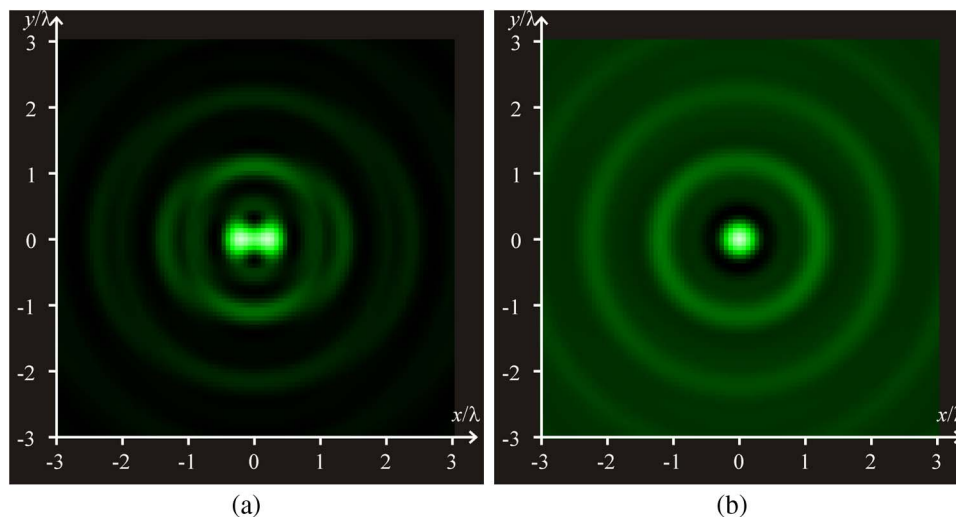

Fig. 5. (Color online) Patterns of the near-surface (a) intensity and (b) the power flux generated at distance $\lambda/20$ using a binary microaxicon of period $T = \lambda$.
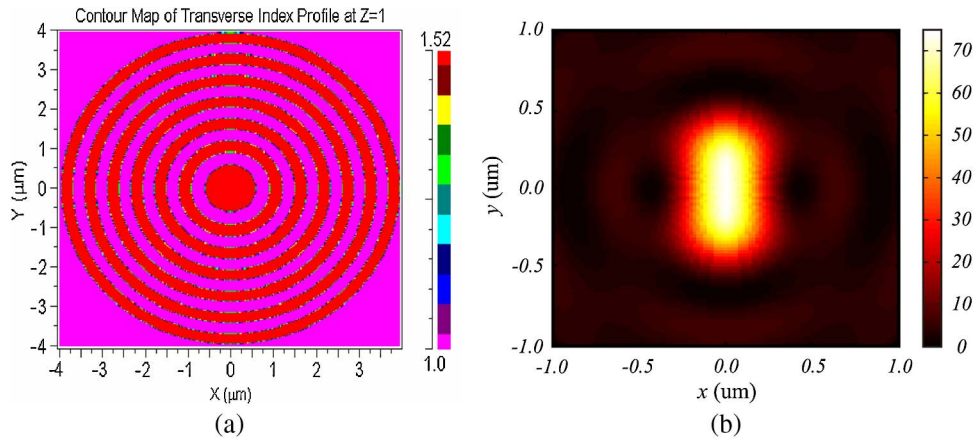
Fig. 6. (Color online) (a) Template of a ZP with a one-wavelength focal length, $f = \lambda$ and (b) the intensity pattern in the focal plane. The polarization is along the y-axis.
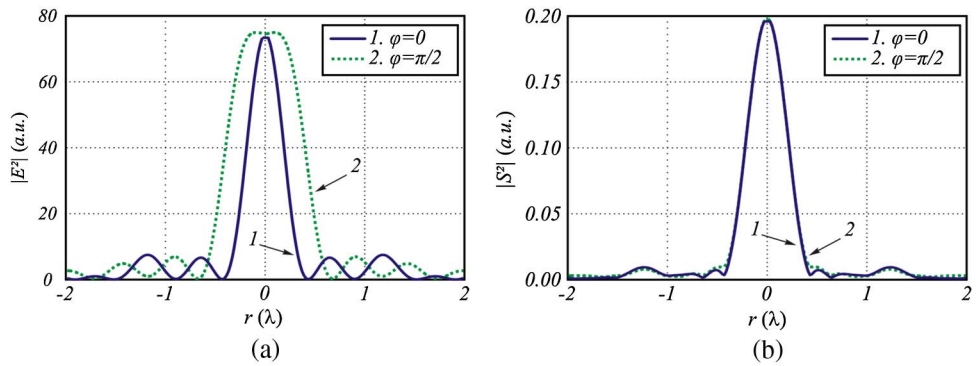

Fig. 7. (Color online) Patterns of (a) the intensity and (b) the power flux in the focal plane for the space step $\Delta r = \lambda/50$. The profiles are mapped along the x-axis ($\varphi = 0$) and y-axis ($\varphi = \pi/2$).

Table 1. Focal Spot Size

	FWHM$_x(\varphi = 0)$, λ	FWHM$_y(\varphi = \pi/2)$, λ	DOF, λ
Intensity	0.42 ± 0.01	0.84 ± 0.01	0.86 ± 0.01
Modulus of Poynting vector's projection onto the z-axis	0.45 ± 0.01	0.45 ± 0.01	—
NSOM-based experiment	0.44 ± 0.02	0.52 ± 0.02	0.75 ± 0.02

radius $\omega = 7\lambda$ with a binary ZP of the incident wavelength's focus, $f = \lambda$, radius $R = 20\lambda = 10.64$ μm, and refractive index $n = 1.52$. The template of such a ZP is shown in Fig. 6. The ZP has NA = 0.997. The estimated focusing efficiency is 42%.

The ZP radii [Fig. 6(a)] were calculated by the well-known formula $r_m = (m\lambda f + m^2\lambda^2/4)^{1/2}$, where m is the zone radius number. The simulation was performed using the body of revolution (BOR)-FDTD method [14] and included the comparative analysis of results derived for different space discretization values. Figure 6(b) depicts the focal intensity pattern in pseudocolors.

Figure 7 shows the Cartesian focal spot's profiles on the x-axis ($\varphi = 0$) and y-axis ($\varphi = \pi/2$): (a) intensity and (b) power flux. From Figs. 6(b) and 7(a), the
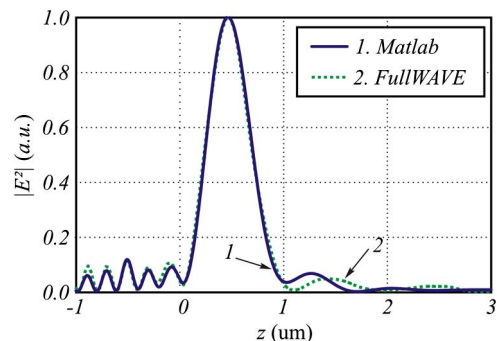

Fig. 8. (Color online) Comparison of the ZP-aided intensity profiles along the optical axis produced by the BOR-FDTD Matlab simulation (curve 1) and FDTD-based FullWAVE simulation (curve 2).

focal spot intensity is seen to form an ellipse. At the same time, Fig. 7(b) shows that the power flux distribution across the focal spot forms a circle. In Table 1, two upper rows show the FWHM for the intensity (row 1) and for the power flux (row 2).

Figure 8 depicts the intensity profiles calculated by the BOR-FDTD method in Matlab [14] (curve 1) and by the FDTD method in the FullWAVE software [22] (curve 2). The DOF values are shown in the column 4 of Table 1.

B. Experiment

The high-quality ZP was fabricated by a lithographic procedure in a ZEP resist ($n = 1.52$). The atomic force microscope (AFM) images of the ZP in Fig. 9 present (a) the side views and (b) the top view. The ZP parameters are as follows: relief depth, 510 nm; diameter, 14 μm; and the outermost zone, $0.5\lambda = 266$ nm. The ZP has 12 rings and a central disk.

The propagation of a linearly polarized Gaussian beam of wavelength $\lambda = 532$ nm through the ZP of focus $f = \lambda$ was experimentally studied using NSOM Ntegra Spectra (NT-MDT), as shown in Fig. 10(a). The NSOM arrangement is shown in Fig. 10(b). A linearly polarized light beam from a 532 nm laser was focused with a lens L1 onto the substrate bottom. Following the diffraction by the ZP, the transverse intensity distributions in the planes parallel to the ZP were measured at different distances (at ~100 nm intervals) using an NSOM tip C. The tip-coupled portion of light was then focused with lens L2 and transmitted through spectrometer S to filter out the irrelevant radiation, before being registered by the CCD camera. The collation of the resulting transverse intensity profiles enables the intensity distribution on the ZP optical axis to be plotted [Fig. 11(a)] and the focal length and DOF to be derived.

The resulting experimental intensity profile on the ZP's optical axis is plotted as a blue crossline markings in Fig. 11(a) (left axis), whereas the focal spot sizes are marked with green vertical segment (right axis). Figure 11(b) shows an example of the focal spot intensity pattern obtained directly on the microscope.

The averaged sizes of the ZP-generated elliptic focal spot are given in row 3 of Table 1. From Fig. 11(a), the intensity peak on the axis is seen to be shifted from the geometric focus plane, $f = \lambda = 532$ nm,
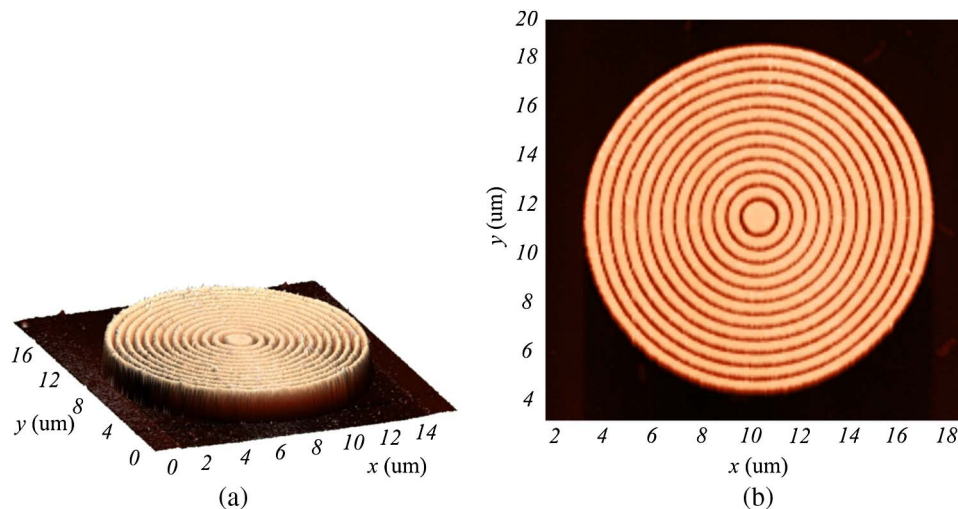

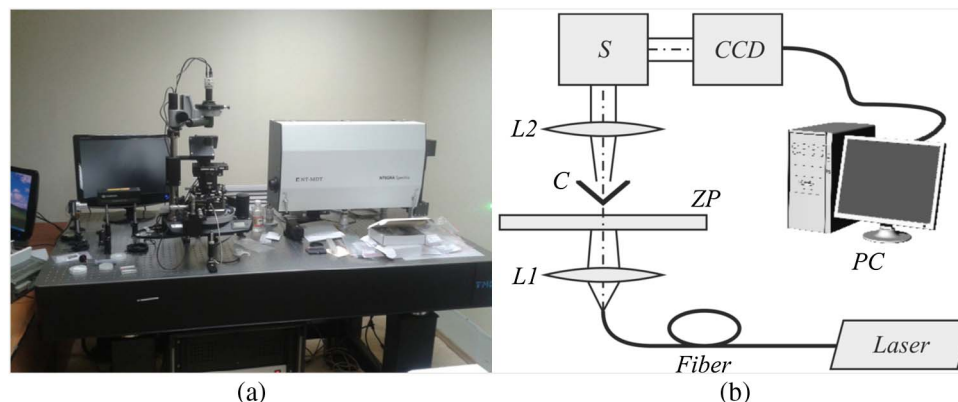Fig. 9. (Color online) AFM images of the ZP under study: (a) side view and (b) top view.

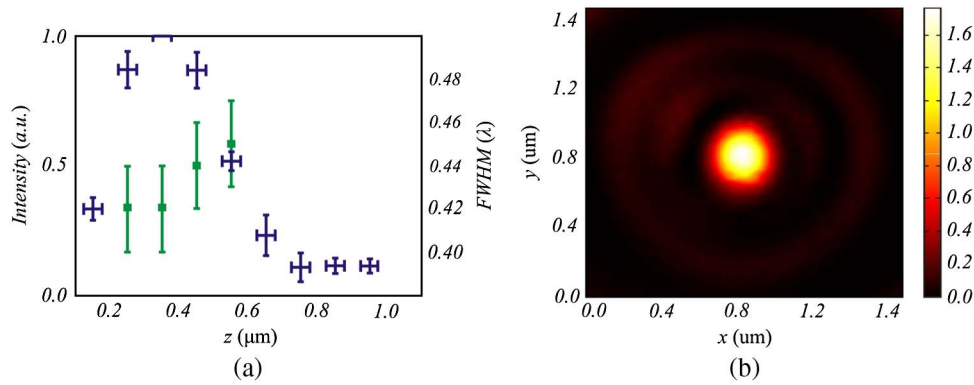Fig. 10. (Color online) (a) NSOM-aided experimental setup and (b) arrangement.

Fig. 11. (Color online) (a) Experimental intensity profile on the optical axis from the ZP in Fig. 9 (blue crossline markings; the left axis) and the focal spot smaller sizes (green vertical segments; the right axis) and (b) the focal spot cross section at the focal length $f = \lambda = 532$ nm (the vertical axis is in the polarization plane).

toward the ZP ($z = 400$ nm). Note that at distance $z = 400$ nm the focal ellipse has the same smaller size for the experiment and for the simulation: FWHM $= 0.42\lambda$.

For comparison, Fig. 12 depicts the profiles of simulated intensity (curve 1) and power flux (curve 3), and the experimentally measured distribution obtained on the NSOM (curve 2). From column two
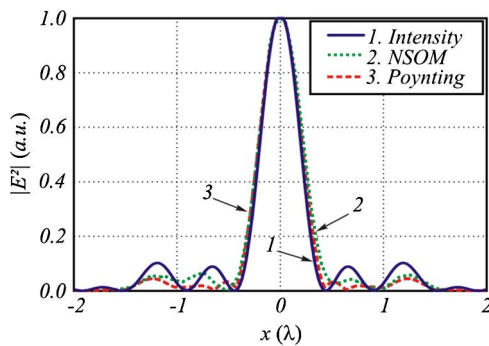

Fig. 12. (Color online) Comparison of the experimental and calculated distribution in the focal spot on the x-axis: calculated intensity profile (curve 1), experimental intensity profile (curve 2), and the calculated distribution of the Poynting vector's absolute value onto the z-axis (curve 3).

of Table 1, the curves are seen to be nearly coincident so that the difference is below the measurement error of $\pm0.02\lambda$. With the difference being only noticeable at sidelobes, it still does not allow one to say unambiguously whether the device really measures the intensity or the power flux, because the sidelobes are somewhat lower than those of the experimental curve for the calculated power flux and somewhat higher for the calculated intensity.

Figure 13 shows the focal spot profiles on the y-axis, which is parallel to the polarization plane, namely, the calculated distribution of power flux on the z-axis (curve 3), the experimental intensity distribution (curve 2), and the calculated intensity distribution (curve 1) taken as a superposition of (a) all components and (b) only transverse components.

Figure 13(a) suggests that the longitudinal intensity component is not measured in the course of the experiment (column 3 of Table 1), because the total intensity peak (FWHM $= 0.84\lambda$) is wider than the experimental peak (FWHM $= 0.52\lambda$) by a value larger than the measurement error $\pm0.02\lambda$. In the meantime, the experimental peak is wider than the calculated peak for the power flux (FWHM $= 0.45\lambda$) by a value larger than the measurement error, thus posing the question: what exactly is measured in the
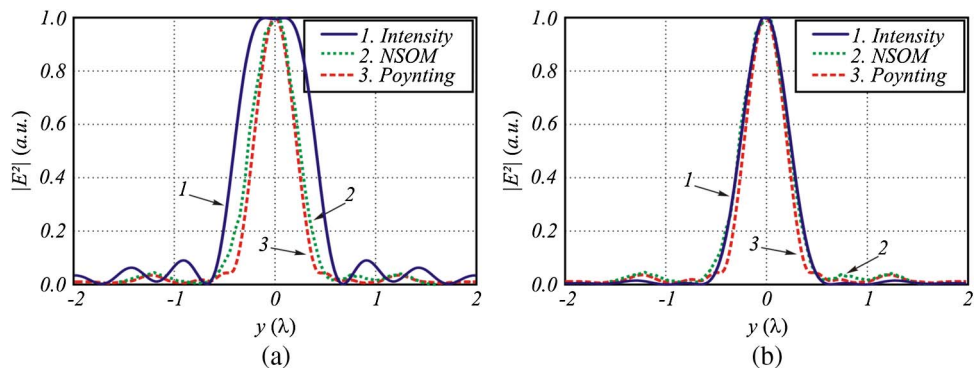

Fig. 13. (Color online) Comparison of the experimental and calculated distribution in the focal spot on the y-axis, which is parallel to the polarization plane: calculated distribution of Poynting's vector absolute value onto the z-axis (curve 3), the experimental intensity distribution (curve 2), and the calculated intensity distribution (curve 1) taken as a superposition of (a) all components and (b) only transverse components.

experiment? In Fig. 13(b), the comparison of the experimental intensity (curve 2) and the transverse intensity $|E_x|^2 + |E_y|^2$ (curve 1) shows the peak widths to be the same: FWHM $= 0.52\lambda$. Therefore, we can unambiguously infer from Fig. 13 that the NSOM with a hollow metal pyramidal tip having a 100 nm aperture and with 70° apex (Fig. 14) measures the energy density in the form of transverse intensity $|E_x|^2 + |E_y|^2$ rather than the power flux or the total intensity $|E_x|^2 + |E_y|^2 + |E_z|^2$. This is the reason why the focal spot ellipse in Fig. 11(b) is less pronounced than the calculated ellipse in Fig. 6(b).

The propagation of the electromagnetic field through the small hole in a metal screen is described within the Bethe–Bouwkamp theory [23–25]. The theory states that a linearly polarized plane tilted wave incident onto the metal screen with a small hole of diameter $a \ll \lambda$ induces an electric dipole found in the perpendicular plane to the slit and a magnetic dipole found in the hole plane. Therefore, when a tilted plane wave **E** is incident on the small hole, the far-field relationship is described by the electric dipole **P** and magnetic dipole **M**:

$$\mathbf{P} = -\frac{4}{3}\varepsilon_0 a^3 (\mathbf{En}_z)\mathbf{n}_z, \quad \mathbf{M} = -\frac{8}{3}a^3[\mathbf{n}_z \times [\mathbf{E} \times \mathbf{n}_z]], \quad (20)$$

where $\mathbf{n}_z$ is the unit vector of the optical axis that is perpendicular to the hole plane. From Eq. (20), the electric dipole is seen to be formed only by the longitudinal component of the electric field **E**. Note, however, that a dipole oriented along the optical axis radiates in the transverse direction, not radiating along the optical axis itself. On the contrary, the magnetic dipole in Eq. (20) is formed only by the transverse electric field components, because the internal vector product on the right-hand side of Eq. (20) equals zero for the longitudinal electric field component. Thus, the longitudinal electric field component is not registered by a photoreceiver put on the optical axis at a distance from the small hole in the metal screen.
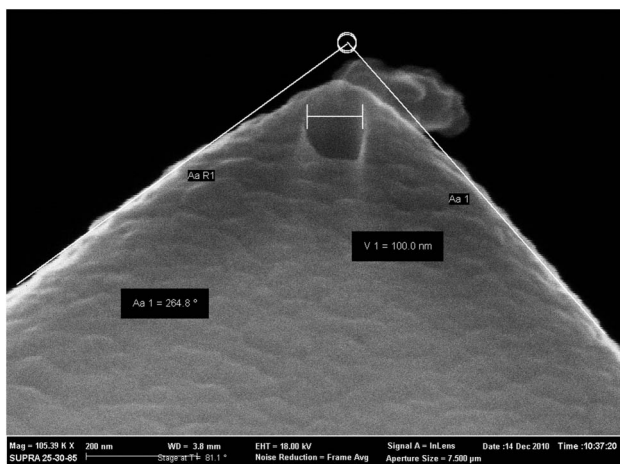
5. Conclusions

Summing up, the following results have been obtained in this work:

By decomposing a vector electromagnetic field in terms of plane waves, the linearly polarized incident wave with high NA has been generally shown to generate a focal spot with the transverse intensity distribution in the form of an ellipse or a dumbbell elongated in a parallel plane to the incident light polarization plane. Meanwhile, the power flux distribution has the form of a circle or an ellipse whose major semi-axis is in a perpendicular plane to the incident beam polarization plane.

The FDTD method simulation has shown that the subwavelength focusing of a linearly polarized wave with the aid of a binary axicon that has the one-wavelength period produces the adjacent focal spot characterized by the "dumbbell" intensity distribution and the circular power flux distribution.

The FDTD simulation has shown that when illuminated by a linearly polarized wave, the glass binary ZP of a one-wavelength focal length produces the intensity focal spot in the form of an ellipse with the smaller diameter FWHM $= (0.42 \pm 0.01)\lambda$, whereas the power flux focal spot has the form of a circle with diameter FWHM $= (0.45 \pm 0.01)\lambda$.

The experiment conducted using the NSOM with a hollow, aluminum-coated pyramidal tip with a 100 nm aperture and a 70° tip apex has shown that when illuminated by a linearly polarized Gaussian beam, the binary ZP of one-wavelength focal length generates a focal spot in the form of a weak ellipse with the Cartesian axis diameters FWHM$_x = (0.44 \pm 0.02)\lambda$ and FWHM$_y = (0.52 \pm 0.02)\lambda$ and the DOF $= (0.75 \pm 0.02)\lambda$. The comparison of the experimental and simulation results suggests that NSOM measures the energy density in the form of transverse intensity, rather than the power flux or the total intensity. The conclusion that the metal tip with a small aperture measures the transverse intensity $|E_x|^2 + |E_y|^2$ can be inferred from the Bethe–Bouwkamp theory.

Fig. 14. Electronic image of the hollow pyramid-shaped metal cantilever tip with a 100 nm aperture and 70° tip apex of the NSOM.

References

1. B. Jia, H. Shi, J. Li, Y. Fu, C. Du, and M. Gu, "Near-field visualization of focal depth modulation by step corrugated plasmonic slits," Appl. Phys. Lett. **94**, 151912 (2009).
2. K. R. Chen, W. H. Chu, H. C. Fang, C. P. Liu, C. H. Huang, H. C. Chui, C. H. Chuang, Y. L. Lo, C. Y. Lin, H. H. Hwung, and

A. Y.-G. Fuh, "Beyond-limit light focusing in the intermediate zone," Opt. Lett. **36**, 4497–4499 (2011).

3. Y. Yu and H. Zappe, "Effect of lens size on the focusing performance of plasmonic lenses and suggestions for the design," Opt. Express **19**, 9434–9444 (2011).

4. Y. Liu, H. Xu, F. Stief, N. Zhitenev, and M. Yu, "Far-field super-focusing with an optical fiber based surface plasmonic lens made of nanoscale concentric annular slits," Opt. Express **19**, 20233–20243 (2011).

5. V. V. Kotlyar, S. S. Stafeev, L. O'Faolain, and V. A. Soifer, "Tight focusing with a binary microaxicon," Opt. Lett. **36**, 3100–3102 (2011).

6. R. G. Mote, S. F. Yu, A. Kumar, W. Zhou, and X. F. Li, "Experimental demonstration of near-field focusing of a phase micro-Fresnel zone plate (FZP) under linearly polarized illumination," Appl. Phys. B **102**, 95–100 (2011).

7. S. S. Stafeev, L. O'Faolain, M. I. Shanina, V. V. Kotlyar, and V. A. Soifer, "Subwavelength focusing with a Fresnel zone plate of 532 nm focal length," Comput. Opt. **35**, 460–461 (2011).

8. J.-S. Ye, G.-A. Mei, X.-H. Zheng, and Y. Zhang, "Long-focal-depth cylindrical microlens with flat axial intensity distributions," J. Mod. Opt. **59**, 90–94 (2012).

9. K. Huang and Y. Li, "Realization of a subwavelength focused spot without a longitudinal field component in a solid immersion lens-based system," Opt. Lett. **36**, 3536–3538 (2011).

10. G. H. Yuan, S. B. Wei, and X.-C. Yuan, "Nondiffracting transversally polarized beam," Opt. Lett. **36**, 3479–3481 (2011).

11. X. Li, Y. Cao, and M. Gu, "Superresolution-focal-volume induced 3.0 Tbytes/disk capacity by focusing a radially polarized beam," Opt. Lett. **36**, 2510–2512 (2011).

12. J. Lin, K. Yin, Y. Li, and J. Tan, "Achievement of longitudinally polarized focusing with long focal depth by amplitude modulation," Opt. Lett. **36**, 1185–1187 (2011).

13. H. Lin, B. Jia, and M. Gu, "Generation of an axially super-resolved quasi-spherical focal spot using an amplitude-modulated radially polarized beam," Opt. Lett. **36**, 2471–2473 (2011).

14. V. V. Kotlyar and S. S. Stafeev, "Modeling the sharp focus of a radially polarized laser mode using a conical and a binary microaxicon," J. Opt. Soc. Am. B **27**, 1991–1997 (2010).

15. J. Martin, J. Proust, D. Gérard, J.-L. Bijeon, and J. Plain, "Plain intense Bessel-like beams arising from pyramid-shaped microtips," Opt. Lett. **37**, 1274–1276 (2012).

16. F. De Angelis, F. Gentile, F. Mecarini, G. Das, M. Moretti, P. Candeloro, M. L. Coluccio, G. Cojoc, A. Accardo, C. Liberale, R. P. Zaccaria, G. Perozziello, L. Tirinato, A. Toma, G. Cuda, R. Cingolani, and E. Di Fabrizio, "Breaking the diffusion limit with super-hydrophobic delivery of molecules to plasmonic nanofocusing SERS structures," Nat. Photonics **5**, 682–687 (2011).

17. E. T. F. Rogers, J. Lindberg, T. Roy, S. Savo, J. E. Chad, M. R. Dennis, and N. I. Zheludev, "A super-oscillatory lens optical microscope for subwavelength imaging," Nat. Mater. **11**, 432–435 (2012).

18. A. Bouhelier, M. Beversluis, A. Hartschuh, and L. Novotny, "Near-field second-harmonic generation induced by local field enhancement," Phys. Rev. Lett. **90**, 013903 (2003).

19. B. Jia, X. Gan, and M. Gu, "Direct observation of a pure focused evanescent field of a high numerical aperture objective lens by scanning near-field optical microscopy," Appl. Phys. Lett. **86**, 131110 (2005).

20. B. Jia, X. Gan, and M. Gu, "Direct measurement of a radially polarized focused evanescent field facilitated by a single LCD," Opt. Express **13**, 6821–6827 (2005).

21. Z. Lin, J. M. Steele, W. Srituravanch, Y. Pikus, C. Sun, and X. Zhang, "Focusing surface plasmons with a plasmonics lens," Nano Lett. **5**, 1726–1729 (2005).

22. http://www.rsoftdesign.com/products.php?sub=Component+Design&itm=FullWAVE.

23. L. Novotny and B. Hecht, *Principles of Nano-Optics* (Cambridge University, 2006).

24. K. A. Michalski, "Complex image method analysis of a plane wave-excited subwavelength circular aperture in a planar screen," Prog. Electromagn. Res. **27**, 253–272 (2011).

25. J. H. Wu, "Modeling of near-field optical diffraction from a subwavelength aperture in a thin conducting film," Opt. Lett. **36**, 3440–3442 (2011).